Supporting Information for the Article

Reaction Network of CO_2 Hydrogenation into C_{1-2} Oxygenates and Its BEP Relationships

Mikhail V. Polynski[1], *Sergey M. Kozlov**[1]

[1] Department of Chemical and Biomolecular Engineering, National University of Singapore, 4 Engineering Drive 4, Singapore 117585, Singapore.

Corresponding Authors

* (S.M.K.) sergey.kozlov@nus.edu.sg

Table of Contents

S1. Elementary Steps Preselected in the Reaction Network

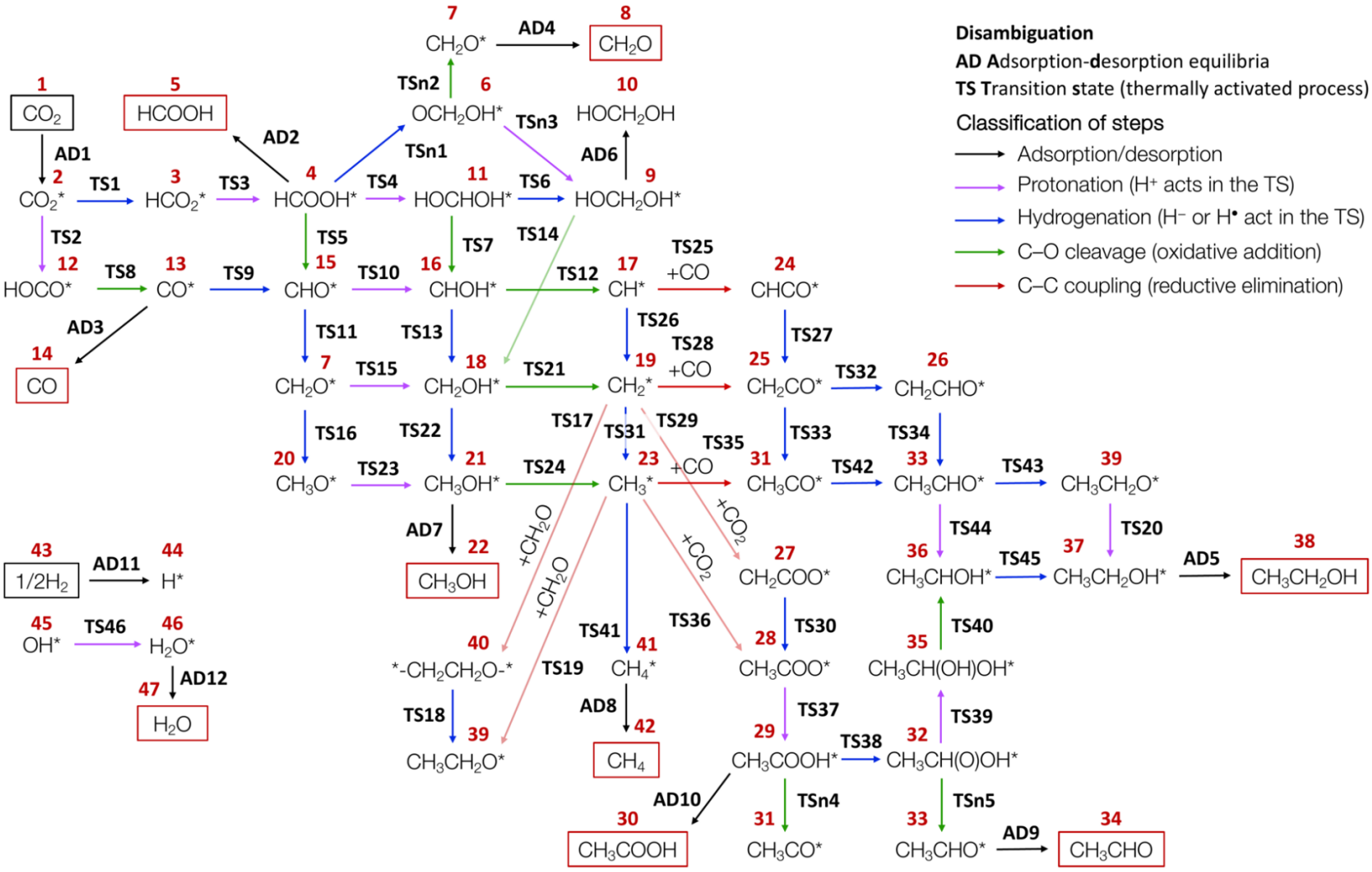

Figure S1. Result of the pre-selection of elementary steps based on the criterion outlined in Section 2.1 and Figure 1a.

Intermediate labels (in red) and TS labels (in bold black) mark data points in the supporting spreadsheet and ZIP archive. Dissociative adsorption was considered for H_2.

A more detailed discussion of the rationale for our focus on C-C coupling steps involving at least one highly stable intermediate and neglect of C-C coupling steps involving two unstable species is given below.

The rate of coupling steps between surface intermediates in a reaction $A^* + B^* \rightarrow AB^* + *$ can be calculated as

$$r_{AB} = k_{AB} * \theta_A \theta_B = K \cdot \exp\left\{-\frac{\Delta G_{AB}^{\ddagger}}{k_B T}\right\} * \theta_A \theta_B \qquad (1)$$

Where K is the prefactor, $\Delta G_{AB}^{\ddagger} > 0$ is the activation energy, k_B is the Boltzmann constant, and θ is the surface concentration of species A or B, which under chemical equilibrium conditions is governed by their Gibbs free energy, ΔG_n, relative to the molecules in the reaction feed:

$$\theta_B \sim \exp\left\{-\frac{\Delta G_n^B}{k_B T}\right\} \qquad (2)$$

As a result, the C-C coupling rate depends exponentially on the relative Gibbs free energy of the coupling partner:

$$r_{AB} \sim \exp\left\{-\frac{(\Delta G_{AB}^{\ddagger} + \Delta G_n^B)}{k_B T}\right\} * \theta_A \qquad (3)$$

As described in the main text, our analysis suggests that C-C coupling between CH_x species and CO_2 with barriers $\Delta G_{CHx-CO2}^{\ddagger} < 1$ eV is one of the main pathways towards the formation of C_2 species. Moreover, CO_2 is highly abundant in the system with relative Gibbs free energy of CO_2* equal to $\Delta G_n = 0.06\ eV$. Besides CO and CH_2O comprehensively considered in our analysis, other potential C-C coupling partners such as CHO*, CHOH*, and CH_2OH* exhibit ΔG_n values of 1.01, 1.30, and 0.86 eV, respectively. Thus, C-C coupling barriers of these species with CH_x should be below 0.2 eV in order to result in a similar reaction rate r_{AB} as the coupling between CH_x and CO_2. Since we find such low magnitudes of C-C barriers to be unlikely, we omit comprehensive consideration of C-C coupling steps involving CHO*, CHOH*, and CH_2OH* intermediates in our analysis.

It should be noted that the list of relatively stable C1 species that could participate in C-C coupling also includes CH_3* and HCOO*. The former species are included in the set of CH_x intermediates, for which all C-C coupling steps are studied systematically. In turn, coupling of the formate intermediate (HCOO*) with other species is deemed unlikely because formate is a resonance-stabilized carboxylate and is therefore a weak nucleophile toward C-electrophiles. Moreover, coupling of HCOO* with other reaction intermediates would result in the formation of a gem-diol(ate)-type intermediates, which are highly unstable.

S2. Computational Details

Initial geometries were obtained using the GFN1-xTB Hamiltonian[1] within the XTB ASE[2] calculator, setting the electronic temperature to 300.0 K. Geometry optimization employed the BFGS algorithm with line search, targeting a convergence criterion of 0.01 eV/Å for the maximal force component on initial and final states. Transition states were identified with the scaled and dynamic NEB method (DyNEB),[3] using the FIRE algorithm[4] with a force criterion of 0.03 eV/Å. Additional semi-empirical setup details are in the supplementary ZIP archive. All structures underwent vibrational frequency calculations for non-metal atoms to identify potential energy surface minima and saddle points associated with adsorbate transformations (displacement = 0.01 Å, modes = 2). The analysis confirmed the absence of imaginary modes in minima and the presence of a single imaginary mode along the reaction coordinate in transition states.

All DFT calculations were performed using the Vienna Ab-initio Simulation Package, version 6.3.2.[5] The generalized gradient approximation with the revised Perdew-Burke-Ernzerhof (revPBE) exchange-correlation functional was employed.[6] We chose this GGA functional for its higher accuracy in describing metallic systems compared to hybrid functionals,[7] and because it has shown reliable results for chemisorption energies on transition-metal surfaces.[8] Moreover, revPBE-D3(BJ) was identified as the *best-performing* GGA functional on the GMTKN55 benchmark superset, which evaluates DFT functionals for their ability to predict basic properties and reaction energies in both small and large systems, isomerization reactions, activation barrier heights, and non-covalent interactions.[9] The general accuracy of the underlying functional was of paramount importance in our case, as the modeled systems exhibited all key aspects covered by GMTKN55, namely, reaction energy prediction, barrier height estimation, comparison of energies of isomeric $C_xH_yO_z$ compounds, and numerous non-covalent interactions. Therefore, the multipurpose GGA functional revPBE-D3(BJ) was selected for its demonstrated accuracy and its lower computational cost relative to meta-GGA, hybrid, and non-local van der Waals-corrected GGA functionals. The benchmarking of the results calculated using revPBE-D3(BJ) with the meta-GGA values obtained in another study is given in Supplementary Section S8.

A plane-wave energy cutoff of 415 eV (ENCUT = 415) was used to ensure accurate results for systems including both metal and non-metal elements. The projector augmented-wave method was applied to describe the interactions between core and valence electrons.[10] The DFT-D3 scheme with Becke-Johnson damping (IVDW = 12) was used to account for dispersion forces.[11,12]

Spin polarization was included in all calculations (ISPIN = 2) to account for potential magnetization, especially in Pd systems. The Brillouin zone description was restricted to the Γ-point. Electron state occupancies were assigned using the Fermi-Dirac smearing with a width of 0.03 eV. The convergence criterion for electronic self-consistency was set to the stringent values of 10^{-5} eV in geometry optimizations, 10^{-6} eV in transition state optimizations, and 10^{-7} eV in vibrational frequency calculations.

Structural relaxations towards PES minima were performed using the FIRE algorithm[4] or, if an optimization with the former method did not converge, the limited-memory Broyden-Fletcher-Goldfarb-Shanno method[13] implemented in the VASP TST Tools with a force convergence criterion of 0.01 eV/Å. All calculations were performed with a maximum of 400 electronic steps allowed per self-consistent field cycle. The real-space projection of wavefunctions was disabled (LREAL = .FALSE.) to improve accuracy, and the plane-wave projection scheme (LPLANE = .TRUE.) was employed for efficient parallelization. Symmetry operations were disabled (ISYM =

-1) to allow for full relaxation of the structure without symmetry constraints. The calculations included contributions from the non-spherical components of the gradient corrections for the PAW spheres (LASPH = .TRUE.), which is essential for the accurate treatment of transition metal compounds.

Systems were modeled in orthorhombic cells with dimensions ensuring at least 10.0 Å separation between periodic images of Cu_{79} or Pd_{79} nanoparticles. The DIMER method implemented in VTST tools was used for TS optimization with a force convergence criterion of 0.03 eV/Å.[14–17] All other parameters in DIMER calculations matched those employed in the geometry optimization procedures described above. Diffusion transition states were identified using the DIMER method at the DFT level. We analyzed imaginary modes in the PES minima and perturbed initial geometries along normal mode vectors, starting with the lowest mode values to sample the directions of least curvature preferentially until convergent TS optimization was achieved. Calculated vibrations of non-metal atoms confirmed that all saddle points had only one imaginary mode corresponding to the reaction coordinate. In PES minima, minor imaginary frequencies ($< 50i$ cm^{-1}) associated with translational or rotational movement of physisorbed species like CH_4 or CO_2 were occasionally observed. These values were taken as the moduli of the corresponding complex numbers in thermochemical calculations due to the stringent convergence criteria used in geometry optimizations.

Thermochemical calculations were conducted using the Thermo module of ASE, including only harmonic vibrational terms for nanoparticle systems and within the ideal gas, rigid rotor, and harmonic oscillator approximations for gas-phase species. IUPAC standard pressure (1 bar) and temperature (273.15 K) were selected in thermochemical calculations.

A high-throughput reaction network exploration workflow was employed, integrating semi-empirical calculations with DFT methods in a multistep process (see Figure S2 below). This approach facilitates the efficient exploration of reaction networks by fast generation of initial structures for DFT calculations. Pre- and post-reaction intermediates are optimized using the GFN1-xTB Hamiltonian within the ASE framework, employing the BFGS algorithm with line search. The DyNEB method, also implemented in ASE, locates approximate transition states, with the FIRE algorithm ensuring convergence. All stationary points are then validated through vibrational frequency analysis at the semi-empirical level to check whether minima show no imaginary frequencies and transition states are identified by a single imaginary mode.

The imaginary mode from the semi-empirical transition state corresponding to the desired reaction coordinate was used to generate the MODECAR file, i.e., the normal mode vector used as the search vector in the subsequent DIMER calculation with VASP. After obtaining the DFT-optimized transition state geometry, perturbations along the imaginary mode in both directions were performed. These perturbations generated structures that were optimized at the DFT level to find the final pre- and post-reaction states. Following these optimizations, all DFT-optimized stationary points underwent further vibrational frequency analysis to confirm their nature.

The Nelder-Mead simplex algorithm, implemented in SciDAVis with a tolerance of 10^{-4}, was used to establish BEP relationships as follows. First, the data were split into two distinct clusters, e.g., hydrogenations of sp^2 vs. sp^3 carbon, protonation of $RCOO^-$ vs. RO^- groups, or C–C couplings through metathesis vs. nucleophilic addition to sp^2 carbon, and each cluster was fitted separately. Figure 4 reveals that within each reaction class, these clusters share similar slopes in linear regression (namely, the calculated slopes are within 95% confidence intervals of each other).

Consequently, we fixed the slope in both fittings on their average value and re-fitted the intercepts. For C–O cleavages, where only one TS type was identified, a single fit sufficed.

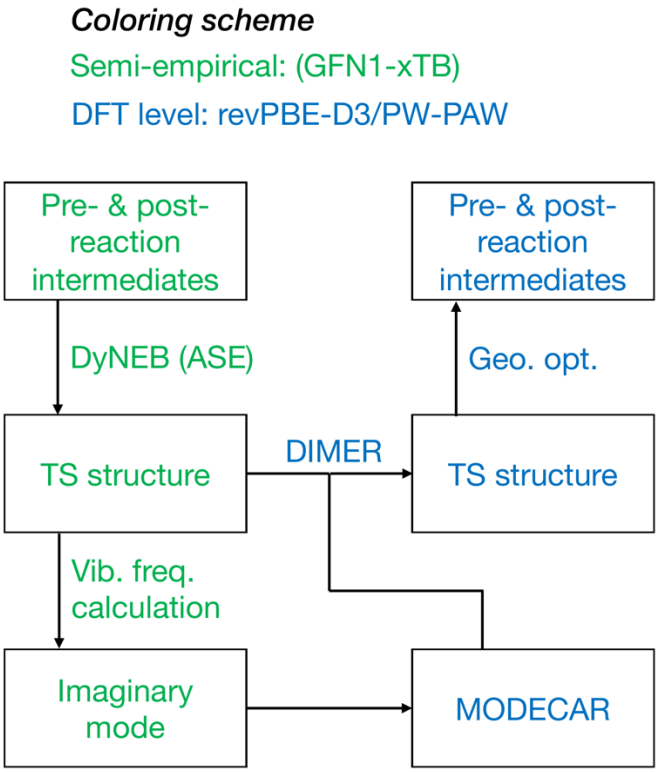

Figure S2. Schematic representation of the multistep computational workflow.

Green: calculations (arrows) and results (rectangles) obtained using the semi-empirical method; blue: calculations and results obtained at the DFT level.

S3. Catalytic Reaction Network on Pd

The catalytic reaction network for CO_2 hydrogenation on Pd is shown in Figure S3 as a directed graph. Unlike Cu, on Pd, the formate pathway of CO_2 activation is less favored kinetically than the RWGS pathway, with the barrier of CO_2* hydrogenation into HCOO* being ~0.2 eV higher than the barrier for CO_2* protonation into HOCO*. Subsequent C–O bond cleavage in HOCO* is notably facile, with a barrier of 0.63 eV. This step leads to the formation of the most stable intermediate in the network, CO*, with ΔG_n equal to −1.05 eV relative to non-mixed CO_2^{gas} and H_2^{gas}. Subsequent CO desorption requires a significant Gibbs free energy change of +1.76 eV, which is higher than the activation barrier for its hydrogenation:

$$CO^* + H^* \rightarrow CHO^* \qquad (\Delta G^{\ddagger} = 1.58 \text{ eV}).$$

Therefore, CO acts as a catalyst poison, accumulating on the Pd surface, which is consistent with experimental findings.[18] Additionally, under high CO* coverage, Pd can leach into the gas phase.[19]

Besides facile CO formation, Pd shows a clear disadvantage in the selectivity of CO_2 hydrogenation due to the increasingly facile hydrogenation along the CH* → CH_2* → CH_3* → CH_4* pathway:

$$CH^* + H^* \rightarrow CH_2^* \ (\Delta G^{\ddagger} = 1.02 \text{ eV}),$$

$$CH_2^* + H^* \rightarrow CH_3^* \ (\Delta G^{\ddagger} = 0.81 \text{ eV}),$$

$$CH_3^* + H^* \rightarrow CH_4^* \ (\Delta G^{\ddagger} = 0.59 \text{ eV}).$$

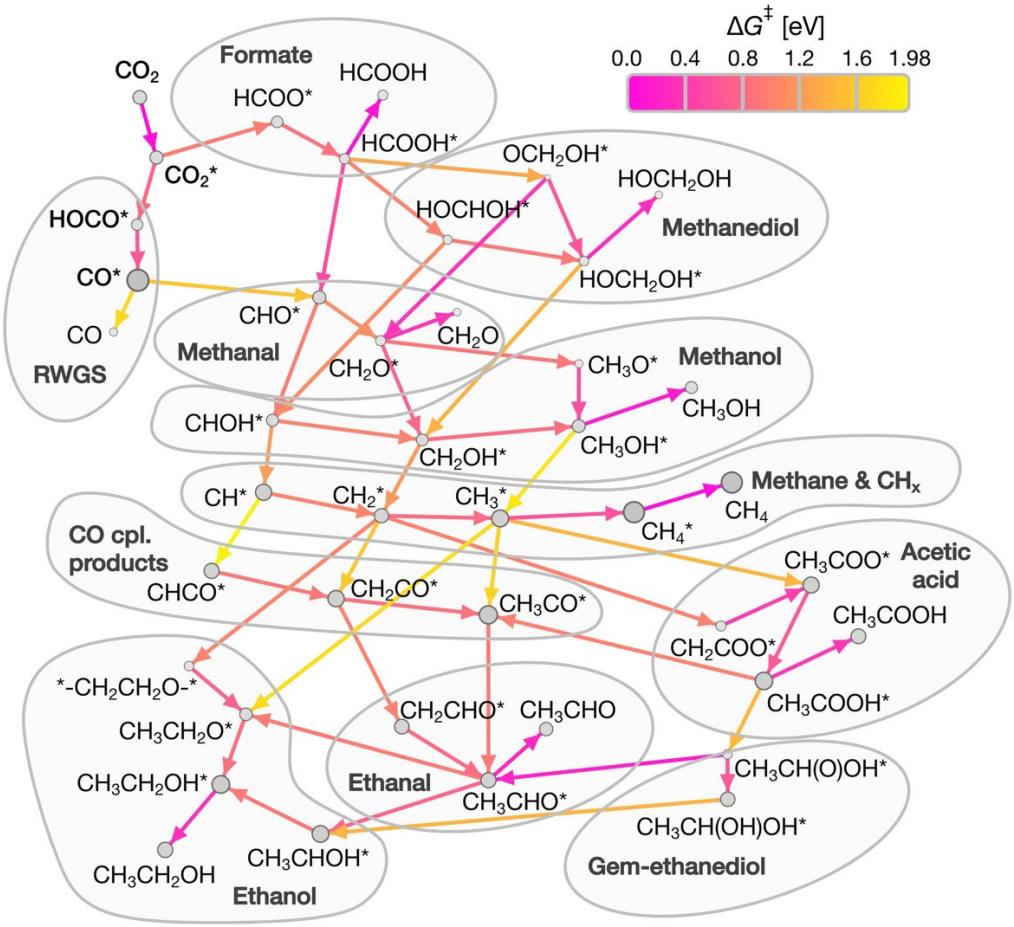

Figure S3. Catalytic reaction network on Pd depicted as a directed graph.

Edge color codes: absolute barriers calculated relative to the respective initial states, $\Delta G^{\ddagger}$, encoded in edges. The size of the node circles reflects relative stability, measured by ΔG_n, where the largest nodes indicate the highest stability and *vice versa*. Key intermediates (CO_2*, HOCO*, CO*) are marked with semi-bold typeface.

Moreover, similarly to Cu, Pd poorly catalyzes C–O cleavages (see yellow or orange nodes connecting clusters in Figure S3). However, it also lacks the ability to facilitate C–C couplings, with even the easiest coupling still featuring a relatively high barrier:

$$CH_2^* + CO_2^* \rightarrow CH_2COO^* \qquad (\Delta G^{\ddagger} = 1.00 \text{ eV}).$$

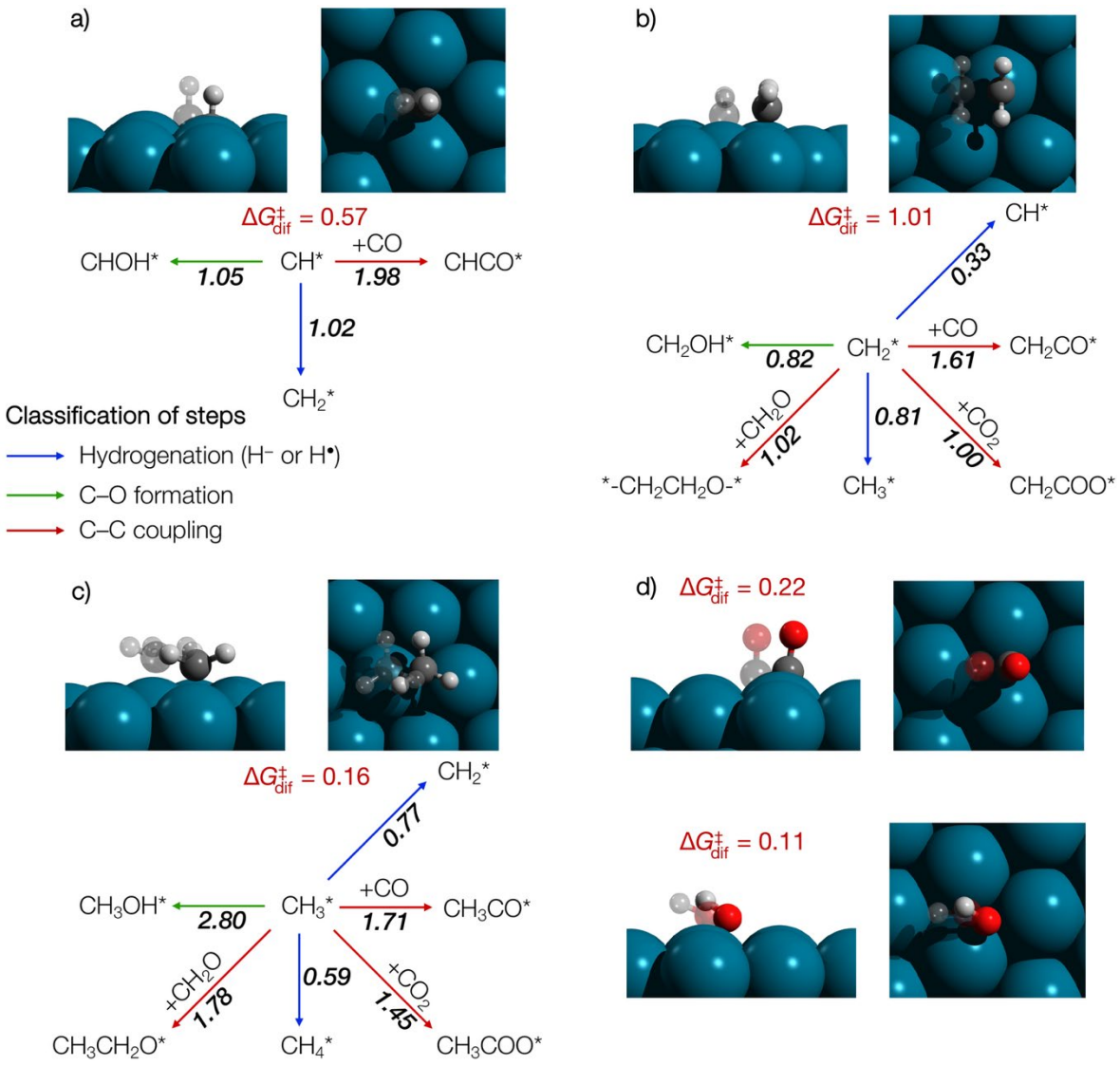

Figure S4. Diffusion transition states (opaque) and minima on the PES (translucent) on the (111) facet of a Pd nanoparticle.

Intermediates considered: a) CH*; b) CH_2*; c) CH_3*; d) CO* and OH*. Only the relevant areas on the NP are shown. Diffusion barriers $\Delta G^{\ddagger}$ are shown in red, alongside the barriers for elementary steps involving the respective species in the reaction network; Pd is represented in dark blue, O in red, C in dark grey, and H in light grey. All values are in eV.

Although Pd is a more strongly binding metal than Cu, it still exhibits facile diffusion of most adsorbates. Figure S4 indicates that CH*, CH_3*, CO*, and HO* can migrate with barriers well below those for hydrogenation, C–C coupling, and C–O coupling (and cleavage; see the supplementary spreadsheet) steps involving these species. However, CH_2* diffusion shows a high barrier of 1.01 eV, matching or surpassing some of the reaction barriers in the reaction steps involving CH_2. At the same time, the data in the supporting spreadsheet indicate that the diffusion of species attached to the surface via a sp^2-hybridized atom between different active sites may not

be essential for their chemical transformations because they react exclusively on the facet without diffusing to the edges. Furthermore, according to the modeling presented above, the most abundant species on the Pd surface are CO*, with the subsequent CO* hydrogenation being kinetically hampered. Thus, the kinetically hampered diffusion of sp^2-hybridized CH_2* is either irrelevant or cannot significantly affect the kinetics of the CO_2 hydrogenation reaction because these species react on the same facet site exclusively.

Despite the abovementioned negative aspects of the reaction network on Pd nanoparticles, they may offer some advantages in multicomponent catalytic systems. First, Pd catalysts easily reduce CO_2 to CO, which can migrate to other catalytically active phases with a low diffusion barrier of 0.22 eV on Pd surfaces. Second, as a relatively electronegative metal,[20] Pd enhances protonation steps by facilitating H* to act as H^+ (Section 2.4), which is particularly helpful for OH* transformation into physisorbed H_2O, which can be readily removed from the surface for active site regeneration.

S4. Atomistic Model and Reference States

All reaction intermediates were modeled at the center of the (111) facet (Figure S5a), representing the most stable and abundant surface on transition metal catalysts with fcc structure. Each intermediate was assumed to bind at the hollow, bridge, or top sites of the triad of atoms highlighted in blue. After DFT geometry optimization (see Section S1), most transition states were located on the facet and did not involve edge atoms (marked with a dashed line in Figure 1b), except the transition states discussed in the main text. As discussed in Section 2.3, facile surface diffusion was calculated for all surface species on Cu and most species on Pd, except CH_2* intermediates with notable diffusion barriers relative to the reaction barriers within the main catalytic network. Somewhat higher diffusion barriers for CH_2* species do not affect the general mechanistic picture but might be important for the development of numerically precise microkinetic models.

Figure S5b illustrates our method for considering the co-adsorption energy of interacting intermediates in the pre-reaction state. Whereas isolated intermediates are treated as discussed in the previous paragraph, their proximity can either increase or decrease the system's (free) energy due to repulsive or attractive co-adsorption interactions, respectively. Stabilizing co-adsorption effectively raises the activation barrier ($\Delta G_1^{\ddagger}$) compared to the energy difference between the obtained transition states and the energies of isolated intermediates. In turn, for destabilizing co-adsorption, the effective barrier is defined from the reference state, including isolated intermediates ($G_2^{\ddagger}$). Thus, the activation energies in this study are determined by:

$$\Delta G^{\ddagger} = \max\left(\Delta G_1^{\ddagger}, \Delta G_2^{\ddagger}\right) \qquad (7).$$

For completeness, the supplementary spreadsheet includes both $\Delta G^{\ddagger}$ activation energies calculated according to equation (7) and $\Delta G_{dir}^{\ddagger}$ barriers calculated from the energies of the pre- and post-reaction states (including coadsorption effects) as resulting from geometry optimization of the transition state perturbed in both directions along the reaction coordinate (sheet “Direct” in the .xlsx table). Importantly, the definition of $\Delta G^{\ddagger}$ according to equation (7), which includes the co-adsorption energy, can be used for monomolecular dissociative steps such as C–O cleavage; however, the (free) energy profile in Figure S5b should be inverted in the horizontal direction in

this case. In addition, the supplementary spreadsheet includes free energies of the transition between in-proximity pre-reaction states to post-reaction states designated as $\Delta G'$ (Figure S5b).

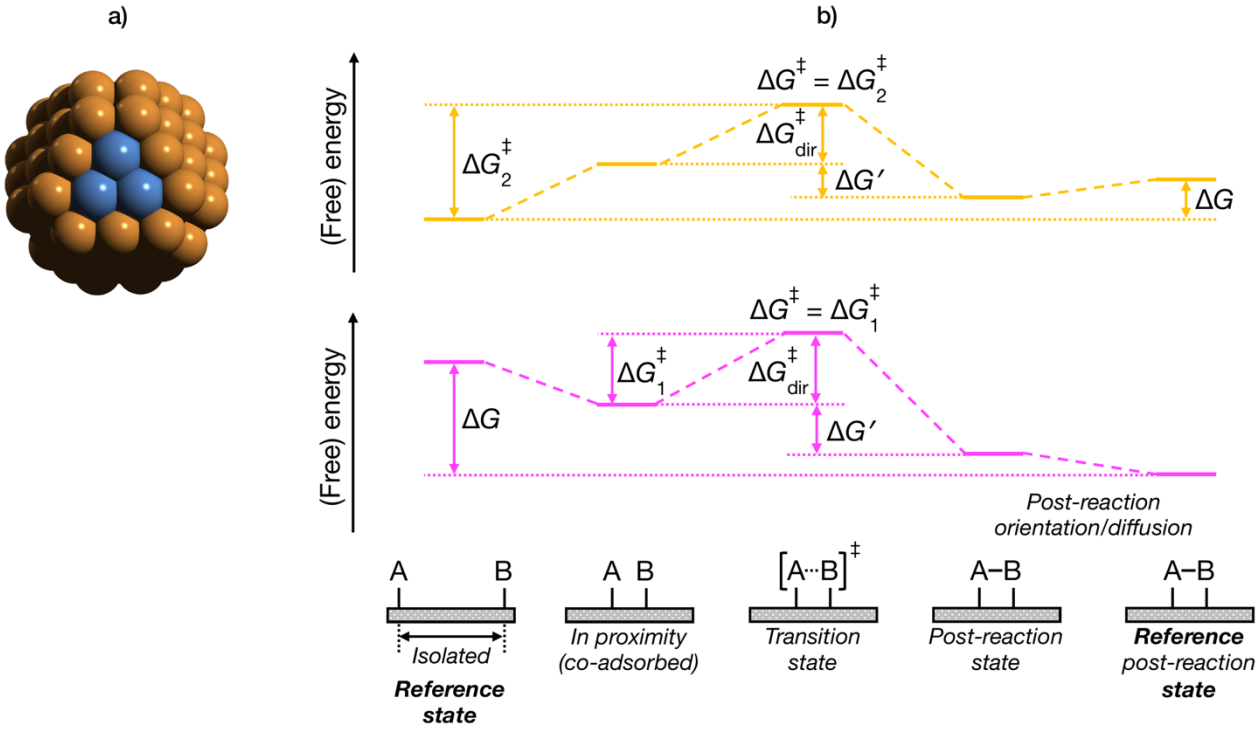

Figure S5. Atomistic model and co-adsorption energy.

a) Metal atoms binding the intermediates in *reference states* are displayed as blue spheres. b) The effect of (magenta) attractive and (yellow) repulsive co-adsorption interactions on the calculated activation barriers in hydrogenation, protonation, and C–C coupling elementary steps. Note that this free energy diagram should be reversed in the horizontal direction for C–O cleavages.

BEP relations are found to be highly sensitive to the definition of free energies for elementary steps (ΔG) used in the analysis because consistent reference states are essential to maintain BEP validity across the reaction network. That is why co-adsorption effects are included during the evaluation of the reaction barriers, not reaction free energies. First, constructing initial and final state energies from Gibbs energies of isolated intermediates ensures that $\Delta G^{\ddagger}$ are defined from a uniform baseline (CO_2^{gas} and H_2^{gas}), in line with the BEP principle. Second, co-adsorption effects vary across catalysts and elementary steps due to the differences in the TS geometry. Including these interactions to activation barriers $\Delta G^{\ddagger}$, rather than reaction energies ΔG, maintains ΔG as a robust descriptor. Third, including co-adsorption effects into ΔG introduces an implicit dependency of the ΔG descriptor on coverage, which complicates BEP analysis and is not considered in most catalyst design studies.

While co-adsorption effects are important and significantly accounted for in $\Delta G^{\ddagger}$, they are dynamic, condition-, and catalyst-dependent, whereas the BEP descriptor, ΔG, should predict intrinsic trends that remain interpretable across diverse catalytic environments. Thus, BEP

relationships for reaction networks are better formulated with reaction free energies referenced to isolated intermediates to ensure scalability and predictive accuracy.

While our definition of reference states for ΔG calculation offers several crucial benefits, it can introduce counterintuitive trends. For example, Figure 4c (left) shows negative BEP slopes for the protonation of RO^- and $RCOO^-$ groups on Cu nanoparticles. $\Delta G'$ values calculated from the in-proximity and direct post-reaction states in Figure S5b yield a common upward trend in the scatter plot connecting reaction barriers and free energies (Figure S6a). The negative slope observed in Figure 4c (left), compared to Figure S6a, is caused by the fact that ΔG without coadsorption effects negatively correlates with the metric $\Delta G' - \Delta G$, which includes co-adsorption and post-reaction orientation effects, as demonstrated in Figure S6b. This exemplifies the tradeoff between incorporating co-adsorption and surface diffusion effects in either $\Delta G^{\ddagger}$ or ΔG.

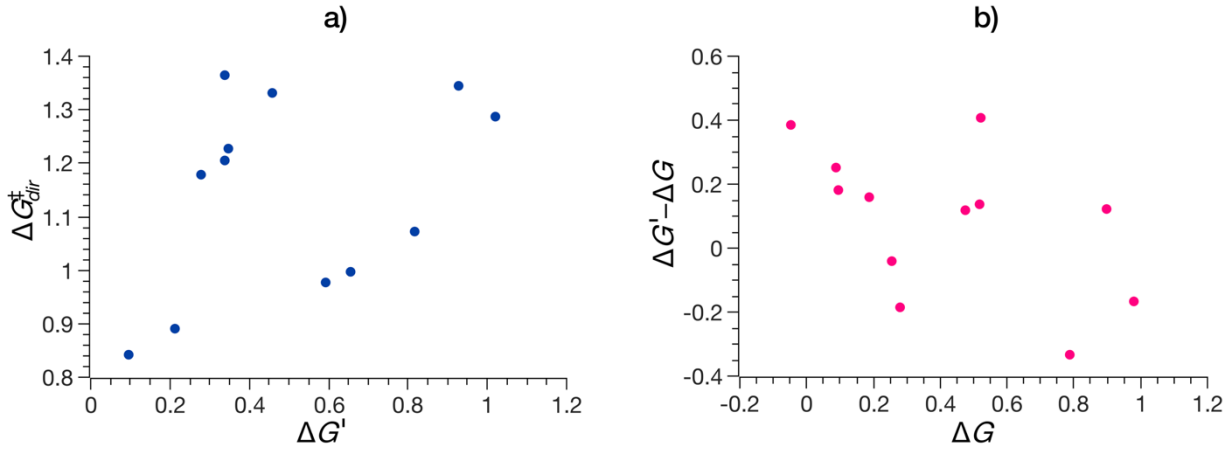

Figure S6. The correlations between thermodynamic and kinetic parameters of all the protonation steps (RO^- and $RCOO^-$ TS classes) on Cu.

a) The common upward trend in the dependence of $\Delta G^{\ddagger}_{dir}$ on $\Delta G'$. b) The difference between $\Delta G' - \Delta G$ plotted against ΔG, showing the effect of co-adsorption and post-reaction orientation/diffusion. The values are in eV. Refer to the text above and Figure S3 for the definitions of the plotted values.

S5. Cu Reaction Network (Numerical Data)

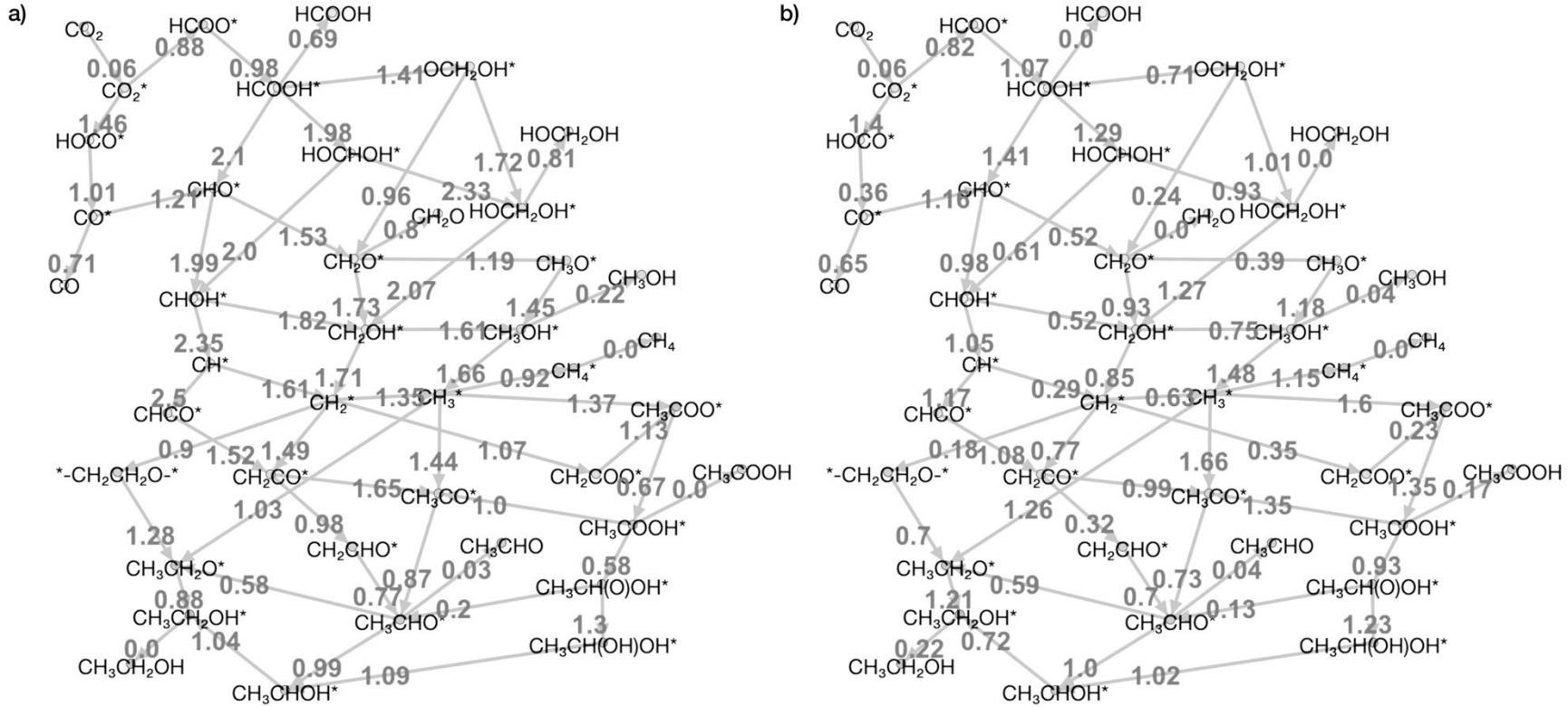

Figure S7. Catalytic reaction network on Cu as a directed graph.

a) Activation energies relative to isolated CO_2^{gas} and H_2^{gas}, $\Delta G_{rel}^{\ddagger}$, encoded in edges; b) absolute barriers calculated relative to their initial states, $\Delta G^{\ddagger}$, encoded in edges. Endergonic adsorption/desorption steps were treated as having $\Delta G_{rel}^{\ddagger}$ or $\Delta G^{\ddagger}$ equal to ΔG, while exergonic adsorption/desorption steps were treated as barrierless. All values are in eV.

S6. Bader Charge Analysis

Our analysis of Bader charges [21] on H atoms in selected Cu and Pd systems illustrates some of the important trends and conventions discussed in the main text. In particular, the higher electronegativity of Pd results in −0.1 charge on H adsorbed compared to −0.26 e^- on H* adsorbed on Cu (Figure S8a and e). In hydrogenation steps (binding of $H^\bullet$ or H^-), the Bader charges on the reacting H atoms in the transition state are indeed either slightly negative or close to zero (Figure S8b, c, f, and g), correctly reflecting the nature of the acting H species. In turn, in protonation steps, e.g., HCOO* protonation, the reacting H* acquires a strongly positive charge in the transition state (Figure S8d and h), confirming the convention of treating hydrogen species acting as H^+.

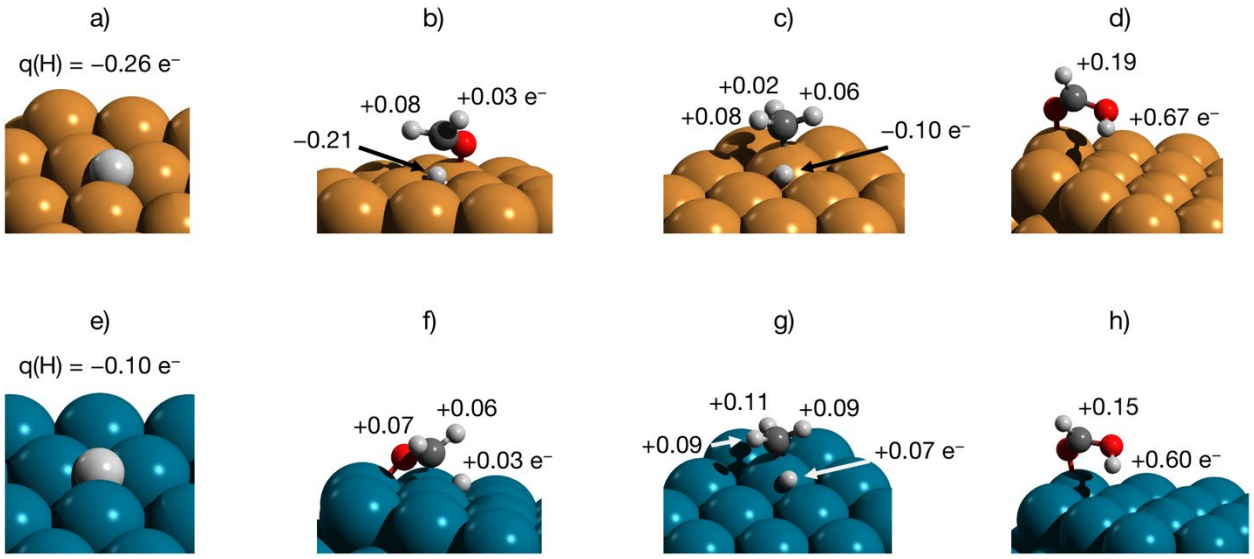

Figure S8. Bader charges on H atoms in selected structures on Cu and Pd catalysts.

Adsorbates considered: a) and d): adsorbed H* species; b) and e): TS in the hydrogenation of **C**H_2O (left) and **C**H_3 (right); c) and f): TS of the protonation of H**C**OO*. Cu is displayed in orange, Pd - dark blue, O - red, C - dark grey, H - light grey.

S7. Visualizations of Selected Transition States

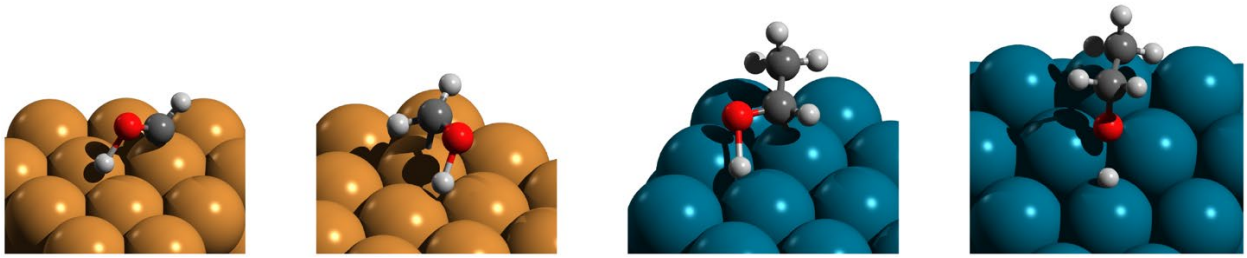

Figure S9. Protonation transition states.

From left to right, transition states in the protonation of CH**O*** on Cu, CH_2**O*** on Cu, physisorbed CH_3CH**O** on Pd, and CH_3CH_2O* on Pd (protonated atom written in bold). Cu is displayed in orange, Pd - dark blue, O - red, C - dark grey, H - light grey.

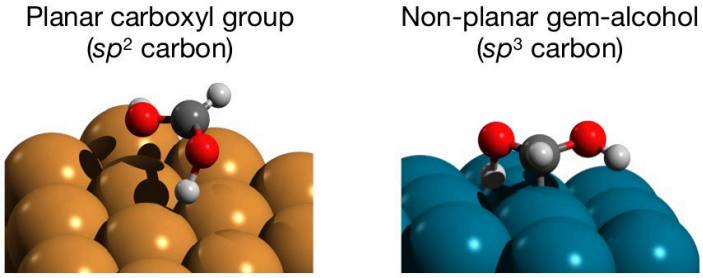

Figure S10. Protonation of HCOOH: transition states.

From left to right, transition states in the protonation of HC**O**OH* on Cu and HC**O**OH* on Pd (protonated atom written in bold). Cu is displayed in orange, Pd - dark blue, O - red, C - dark grey, H - light grey.

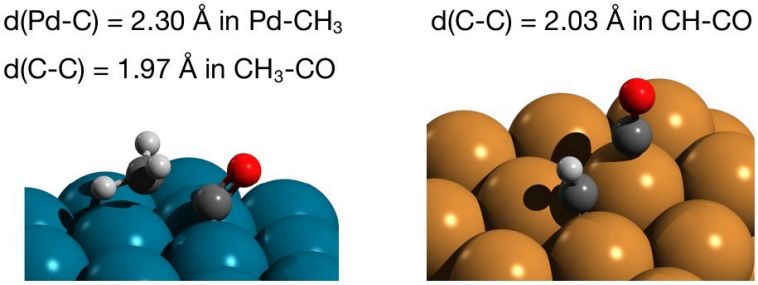

Figure S11. C–C coupling transition states.

From left to right, transition states in the C–C coupling of CH_3 and CO on Pd and in the C–C coupling of CH and CO on Cu. Cu is displayed in orange, Pd - dark blue, O - red, C - dark grey, H - light grey.

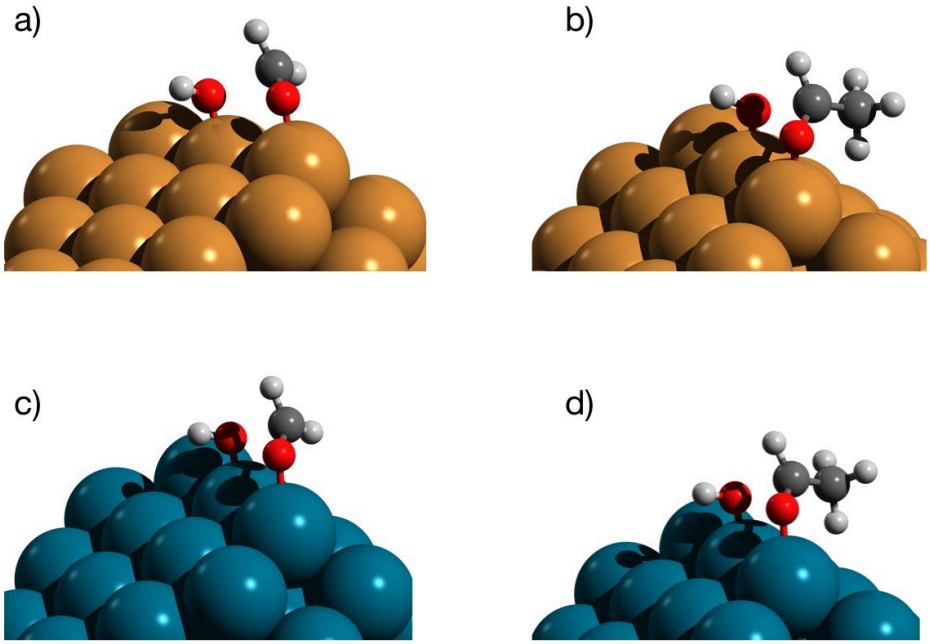

Figure S12. Exceptionally facile C–O cleavage steps.

(a) $OCH_2OH^* \rightarrow CH_2O^* + OH^*$ on Cu; (b) $CH_3CH(O)OH^* \rightarrow CH_3CHO^* + OH^*$ on Cu; (c) $OCH_2OH^* \rightarrow CH_2O^* + OH^*$ on Pd; (d) $CH_3CH(O)OH^* \rightarrow CH_3CHO^* + OH^*$ on Pd. Cu is displayed in orange, Pd - dark blue, O - red, C - dark grey, H - light grey.

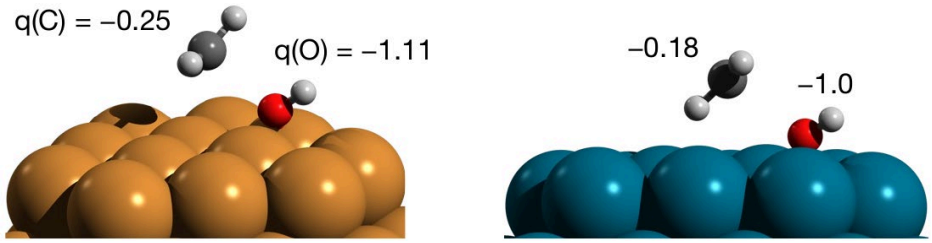

Figure S13. C–O cleavage in CH_3OH on Cu and Pd nanoparticles.

Cu is displayed in orange, Pd - dark blue, O - red, C - dark grey, H - light grey. Bader charges are shown for C and O in both images.

S8. Comparison of Computed Activation Energies with Literature

Table S1. Comparison of selected activation energies for key elementary steps in CO_2 hydrogenation to methanol on Cu surfaces

Elementary step	**This work: $\Delta E^{\ddagger}$ [eV]**	Ref. 22**: $\Delta E^{\ddagger}$ [eV]**	**Deviation****
CO_2* + H* ⟶ HCOO*	0.72 (facet)*	0.85 (111)*	0.13
HCOO* + H* ⟶ HCOOH*	1.08 (facet)	1.16 (111)	0.08
HCOOH* + H* ⟶ OCH_2OH*	0.70 (facet)	1.00 (111)	0.3
OCH_2OH* ⟶ CH_2O* + OH*	0.34 (edge)	0.78 (111); 0.47 (211)	0.13
CH_2O*+ H* ⟶ CH_3O*	0.39 (facet)	0.38 (111)	-0.01
CH_3O*+ H* ⟶ CH_3OH*	1.28 (edge)	1.29 (111); 0.91 (211)	-0.37
CO* + H* ⟶ CHO*	1.20 (facet)	1.13 (111)	-0.07
CHO* + H* ⟶ CH_2O*	0.52 (facet)	0.60 (111)	0.08
CO_2* + H* ⟶ OCOH*	1.41 (edge)	1.67 (111); 1.49 (211)	0.08
CHOH* + H* ⟶ CH_2OH*	0.54 (edge)	0.49 (111); 0.41 (211)	-0.13
CH_2OH* + H* ⟶ CH_3OH*	0.77 (facet)	0.64 (111)	-0.13

* Active site is given in parentheses. ** Values calculated on Cu(111) were compared to the respective values on {111} Cu nanoparticle facets, while values calculated on Cu(211) were compared to the values calculated on Cu nanoparticle edges.

While the high accuracy of the revPBE-D3 functional for general-purpose energetics has been discussed previously,[9] we can further benchmark its performance against higher-accuracy electronic structure calculations for the reactions of interest. For example, Ref. 22 reports several mechanistic pathways for CO_2 hydrogenation to methanol on Cu(111) and Cu(211) slabs calculated using the rMS-RPBEl-rVV10 meta-GGA functional with a nonlocal dispersion correction, which arguably offers improved predictive capability for the CO_2 reaction network by

partially mitigating self-interaction error and by better distinguishing molecular and metallic electronic densities.

Table S1 summarizes a comparison between the revPBE-D3 activation barriers calculated in the present work and the rMS-RPBEl-rVV10 barriers from Ref. 22. For consistency, barriers calculated on Cu(111) in Ref. 22 are compared to the values on the {111} facet sites of Cu nanoparticles, while barriers calculated on Cu(211) are compared to the values on the edges of Cu nanoparticles (site-matched comparison). Overall, the agreement between the values obtained in this study and the values in Ref. 22 is fairly close despite the different catalyst models (nanoparticle sites vs slab surfaces) and DFT functionals (GGA vs. meta-GGA). Importantly, the comparison also illustrates that low-coordinated edge sites feature significantly lower activation barriers in key elementary steps relative to the close-packed facets. For example, for OCH_2OH^* decomposition to $CH_2O^* + OH^*$, the barrier calculated on nanoparticle edges in our study is 0.34 eV, while Ref. 22 reports 0.78 eV on Cu(111) and 0.47 eV on Cu(211).

In summary, the site-matched mean absolute deviation across the compared barriers is 0.14 eV. Excluding one pronounced outlier ($CH_3O^* + H^*$ to CH_3OH^*), the site-matched MAE decreases to 0.10 eV. Notably, this outlier originates from the strong site sensitivity of this step calculated in Ref. 22, 1.29 eV on Cu(111) vs 0.91 eV on Cu(211), rather than from a systematic DFT functional-level shift. More generally, given that the reported accuracy of GGA and meta-GGA for general-purpose energetics is about 0.35 eV,[9] the deviations observed here are well below the expected uncertainty for semilocal DFT.

S9. References

1 S. Grimme, C. Bannwarth and P. Shushkov, A Robust and Accurate Tight-Binding Quantum Chemical Method for Structures, Vibrational Frequencies, and Noncovalent Interactions of Large Molecular Systems Parametrized for All spd-Block Elements (Z = 1–86), *J Chem Theory Comput*, 2017, 13, 1989–2009.

2 A. Hjorth Larsen, J. JØrgen Mortensen, J. Blomqvist, I. E. Castelli, R. Christensen, M. Dułak, J. Friis, M. N. Groves, B. Hammer, C. Hargus, E. D. Hermes, P. C. Jennings, P. Bjerre Jensen, J. Kermode, J. R. Kitchin, E. Leonhard Kolsbjerg, J. Kubal, K. Kaasbjerg, S. Lysgaard, J. Bergmann Maronsson, T. Maxson, T. Olsen, L. Pastewka, A. Peterson, C. Rostgaard, J. SchiØtz, O. Schütt, M. Strange, K. S. Thygesen, T. Vegge, L. Vilhelmsen, M. Walter, Z. Zeng and K. W. Jacobsen, The atomic simulation environment—a Python library for working with atoms, *Journal of Physics: Condensed Matter*, 2017, 29, 273002.

3 P. Lindgren, G. Kastlunger and A. A. Peterson, Scaled and Dynamic Optimizations of Nudged Elastic Bands, *J Chem Theory Comput*, 2019, 15, 5787–5793.

4 E. Bitzek, P. Koskinen, F. Gähler, M. Moseler and P. Gumbsch, Structural relaxation made simple, *Phys Rev Lett*, 2006, 97, 170201.

5 G. Kresse and J. Furthmüller, Efficient iterative schemes for *ab initio* total-energy calculations using a plane-wave basis set, *Phys Rev B*, 1996, 54, 11169–11186.

6 Y. Zhang and W. Yang, Comment on "Generalized Gradient Approximation Made Simple", *Phys Rev Lett*, 1998, 80, 890.

7 P. Janthon, S. Luo, S. M. Kozlov, F. Viñes, J. Limtrakul, D. G. Truhlar and F. Illas, Bulk properties of transition metals: A challenge for the design of universal density functionals, *J Chem Theory Comput*, 2014, 10, 3832–3839.

8 B. Hammer, L. B. Hansen and J. K. Nørskov, Improved adsorption energetics within density-functional theory using revised Perdew-Burke-Ernzerhof functionals, *Phys Rev B*, 1999, 59, 7413.
9 L. Goerigk, A. Hansen, C. Bauer, S. Ehrlich, A. Najibi and S. Grimme, A look at the density functional theory zoo with the advanced GMTKN55 database for general main group thermochemistry, kinetics and noncovalent interactions, *Physical Chemistry Chemical Physics*, 2017, 19, 32184–32215.
10 G. Kresse and D. Joubert, From ultrasoft pseudopotentials to the projector augmented-wave method, *Phys Rev B*, 1999, 59, 1758–1775.
11 S. Grimme, J. Antony, S. Ehrlich and H. Krieg, A consistent and accurate *ab initio* parametrization of density functional dispersion correction (DFT-D) for the 94 elements H-Pu, *J Chem Phys*, 2010, 132, 154104.
12 S. Grimme, S. Ehrlich and L. Goerigk, Effect of the damping function in dispersion corrected density functional theory, *J Comput Chem*, 2011, 32, 1456–1465.
13 D. C. Liu and J. Nocedal, On the limited memory BFGS method for large scale optimization, *Math Program*, 1989, 45, 503–528.
14 G. Henkelman and H. Jónsson, A dimer method for finding saddle points on high dimensional potential surfaces using only first derivatives, *J Chem Phys*, 1999, 111, 7010–7022.
15 A. Heyden, A. T. Bell and F. J. Keil, Efficient methods for finding transition states in chemical reactions: Comparison of improved dimer method and partitioned rational function optimization method, *Journal of Chemical Physics*, 2005, 123, 224101.
16 J. Kästner and P. Sherwood, Superlinearly converging dimer method for transition state search, *Journal of Chemical Physics*, 2008, 128, 014106.
17 P. Xiao, D. Sheppard, J. Rogal and G. Henkelman, Solid-state dimer method for calculating solid-solid phase transitions, *Journal of Chemical Physics*, 2014, 140, 174104.
18 M. G. T. Burrows and W. H. Stookmayer, The poisoning of a palladium catalyst by carbon monoxide, *Proc R Soc Lond A Math Phys Sci*, 1940, 176, 474–483.
19 C.-R. Chang, Z.-J. Zhao, K. Köhler, A. Genest, J. Li and N. Rösch, Theoretical study on the leaching of palladium in a CO atmosphere, *Catal Sci Technol*, 2012, 2, 2238.
20 C. E. Housecroft and A. G. Sharpe, *Inorganic Chemistry*, Pearson Education Limited, Harlow, 4th editio., 2012.
21 G. Henkelman, A. Arnaldsson and H. Jónsson, A fast and robust algorithm for Bader decomposition of charge density, *Comput Mater Sci*, 2006, 36, 354–360.
22 Y. Cai, R. Michiels, F. De Luca, E. Neyts, X. Tu, A. Bogaerts and N. Gerrits, Improving Molecule–Metal Surface Reaction Networks Using the Meta-Generalized Gradient Approximation: CO_2 Hydrogenation, *The Journal of Physical Chemistry C*, 2024, 128, 8611–8620.